



Delft University of Technology

Illuminating the Electronic Properties of WS₂ Polytypism with Electron Microscopy

van Heijst, Sabrya E.; Mukai, Masaki; Okunishi, Eiji; Hashiguchi, Hiroki; Roest, Laurien I.; Maduro, Louis; Rojo, Juan; Conesa-Boj, Sonia

DOI

[10.1002/andp.202000499](https://doi.org/10.1002/andp.202000499)

Publication date

2021

Document Version

Final published version

Published in

Annalen der Physik

Citation (APA)

van Heijst, S. E., Mukai, M., Okunishi, E., Hashiguchi, H., Roest, L. I., Maduro, L., Rojo, J., & Conesa-Boj, S. (2021). Illuminating the Electronic Properties of WS₂ Polytypism with Electron Microscopy. *Annalen der Physik*, 533(3), Article 2000499. <https://doi.org/10.1002/andp.202000499>

Important note

To cite this publication, please use the final published version (if applicable).

Please check the document version above.

Copyright

Other than for strictly personal use, it is not permitted to download, forward or distribute the text or part of it, without the consent of the author(s) and/or copyright holder(s), unless the work is under an open content license such as Creative Commons.

Takedown policy

Please contact us and provide details if you believe this document breaches copyrights.
We will remove access to the work immediately and investigate your claim.

Illuminating the Electronic Properties of WS₂ Polytypism with Electron Microscopy

Sabrya E. van Heijst, Masaki Mukai, Eiji Okunishi, Hiroki Hashiguchi, Laurien I. Roest, Louis Maduro, Juan Rojo, and Sonia Conesa-Boj*

Tailoring the specific stacking sequence (polytypes) of layered materials represents a powerful strategy to identify and design novel physical properties. While nanostructures built upon transition-metal dichalcogenides (TMDs) with either the 2H or 3R crystalline phases have been routinely studied, knowledge of TMD nanomaterials based on mixed 2H/3R polytypes is far more limited. In this work, mixed 2H/3R free-standing WS₂ nanostructures displaying a flower-like configuration are fingerprinted by means of state-of-the-art transmission electron microscopy. Their rich variety of shape-morphology configurations is correlated with relevant local electronic properties such as edge, surface, and bulk plasmons. Machine learning is deployed to establish that the 2H/3R polytype displays an indirect band gap of $E_{BG} = 1.6^{+0.3}_{-0.2}$ eV. Further, high resolution electron energy-loss spectroscopy reveals energy-gain peaks exhibiting a gain-to-loss ratio greater than unity, a property that can be exploited for cooling strategies of atomically-thin TMD nanostructures and devices built upon them. The findings of this work represent a stepping stone towards an improved understanding of TMD nanomaterials based on mixed crystalline phases.

1. Introduction

Many of the remarkable electronic and optical properties exhibited by transition-metal dichalcogenide (TMD) materials can be traced back to the underlying periodic arrangements of their layers, the so-called stacking sequences.^[1,2] Therefore, identifying and controlling these stacking sequences provides a powerful handle in the quest to design novel TMD-based nanostructures with tailored functionalities.

The most common stacking sequences present in TMDs are the 2H and the 3R polytypes.^[3–5] The 2H phase belongs to the space group P63/mmc and has a unit cell composed of a bilayer following the AA' stacking sequence, a configuration characterized by an inversion symmetry.^[6] The 3R phase belongs instead to the space group R3m and is defined by a bilayer with an AB stacking

sequence, which as opposed to the 2H phase does not exhibit inversion symmetry.^[7] Both crystalline phases are known to display a semiconducting behavior.^[8] While several studies of the structural, optical, and electronic properties of TMDs based on either the 2H or the 3R phases have been reported,^[9–11] much less is known about how these properties are modified in the presence of a mixed 2H/3R polytypism.^[12] Unravelling the implications of such polytypism in TMDs would open new avenues in applications from nanoplasmonics and nanoelectronics to catalysis.^[13–15]

This work reports on the characterization of WS₂ flower-like nanostructures (“nanoflowers”) composed by randomly oriented flakes (the “petals”) arising from a common point (the “stem”). These WS₂ nanoflowers display a rich variety of shape-morphology configurations, such as lying petals and edge-exposed standing petals. Together with their polytypism, this unique feature turns these nanostructures into an ideal laboratory for the study of the modifications of local electronic properties in WS₂.

First of all, aberration-corrected scanning transmission electron microscopy (AC-STEM)^[16] is used to reveal the presence of the 2H/3R polytypism in these nanostructures. Then, the nature of their edge, surface, and bulk plasmonic excitations is fingerprinted by means of spatially-resolved electron energy-loss spectroscopy (EELS).^[17,18] The origin of relevant

S. E. van Heijst, L. I. Roest, L. Maduro, Prof. S. Conesa-Boj
Kavli Institute of Nanoscience

Delft University of Technology
Delft 2628CJ, The Netherlands
E-mail: s.conesaboj@tudelft.nl

Dr. M. Mukai, E. Okunishi, H. Hashiguchi
EMBU JEOL Ltd
Tokyo, Japan

Prof. J. Rojo
Nikhef Theory Group
Science Park 105
Amsterdam 1098XG, The Netherlands
Prof. J. Rojo
Department of Physics and Astronomy
VU Amsterdam
Amsterdam 1081 HV, The Netherlands

 The ORCID identification number(s) for the author(s) of this article can be found under <https://doi.org/10.1002/andp.202000499>

© 2021 The Authors. Annalen der Physik published by Wiley-VCH GmbH. This is an open access article under the terms of the Creative Commons Attribution-NonCommercial-NoDerivs License, which permits use and distribution in any medium, provided the original work is properly cited, the use is non-commercial and no modifications or adaptations are made.

DOI: [10.1002/andp.202000499](https://doi.org/10.1002/andp.202000499)

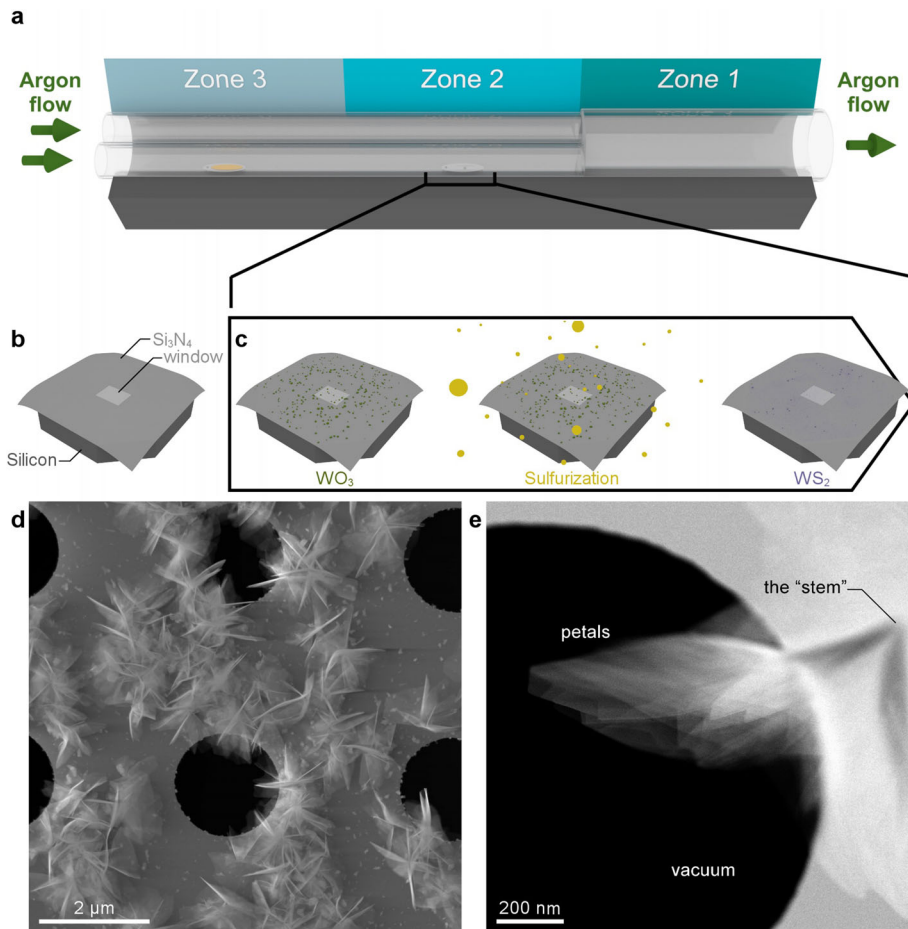


Figure 1. a–c) Schematic illustration of the synthesis procedure for the WS₂ nanoflowers within the three-zone furnace. d) Low-magnification ADF-STEM top-view perspective of the as-grown WS₂ nanostructures illustrating their flower-like morphology. The nanoflowers are grown on top of a holey Si₃N₄ TEM grid. e) ADF-STEM image of one representative WS₂ nanoflower composed by free-standing, randomly oriented WS₂ flakes (petals) protruding from the stem of the flower. This configuration is especially advantageous to eliminate the contributions related to the nanostructure-support film coupling effects.

features in the EELS spectra is traced back to specific structural characteristics of the nanoflowers, and in particular one can identify contributions associated to the surface and interlayer couplings as well as to the edges of the WS₂ petals. The combination of EELS measurements with machine learning is then exploited to chart the ultra-low-loss region ($\Delta E \leq 5$ eV) and determine that the 2H/3R polytype of bulk WS₂ exhibits a semiconductor behavior with an indirect band gap of value of $E_{BG} = 1.6^{+0.3}_{-0.2}$ eV.

Further, EELS spectra recorded in a monochromated TEM^[19] are used to demonstrate the presence of energy-gain peaks in the nanoflowers. These features could be associated with the interactions of collective excitations in the material, such as plasmons, or excitons, with the fast electrons from the beam. Remarkably, for specific nanostructures these energy-gain peaks can become more intense than their energy-loss counterparts, revealing the presence of an underlying mechanism whereby the beam electrons are on average accelerated after crossing the specimen. Such a remarkable feature could be exploited to develop novel cooling strategies for atomically thin TMD nanostructures and for the devices built upon them.

1.1. Mixed 2H/3R Polytypes in WS₂ Nanoflowers: Fabrication and Structural Characterization

Figure 1a displays a schematic diagram summarizing the synthesis of the WS₂ nanoflowers. These nanostructures were directly grown onto a microchip made of silicon as a frame with a silicon nitride (Si₃N₄) window in the middle (see Figure 1b).^[20,21] First, tungsten trioxide (WO₃) powder (50 mg) was dispersed in 1 mL of isopropanol (ISO). Second, a few droplets of the mixed WO₃ and ISO were deposited onto the microchip using a pipette (Figure 1c). As indicated in Figure 1a, a crucible holding 400 mg of sulfur (S) was placed upstream from the microchip in the low-temperature region of the three-zone furnace. An argon gas flow was used both to prevent oxidation as well as to transport the sulfur vapor to the microchip. Further details of the growth procedure can be found in the Supporting Information.

Figure 1d displays low-magnification annular dark-field (ADF) scanning transmission electron microscopy (STEM) images of the as-grown WS₂ nanostructures. It is observed that the nanostructures exhibit flower-like morphologies composed by randomly oriented flakes (the “petals”) arising from a common point

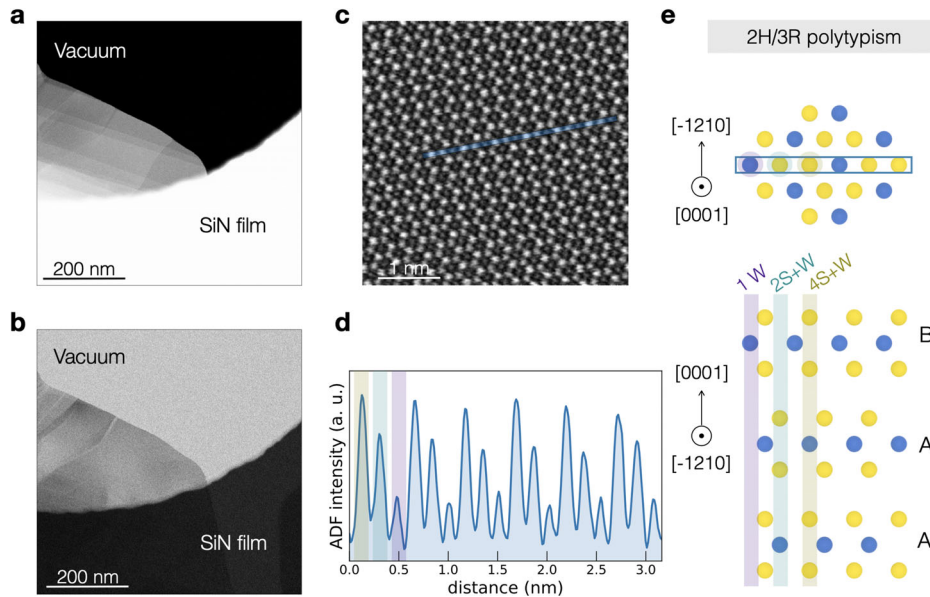


Figure 2. a,b) Low-magnification ADF- and BF-STEM images respectively of a representative WS_2 petal, where the vacuum and SiN film regions are also indicated. The difference in contrast observed in the petal of (a) corresponds to terraces of different thicknesses. c) Atomic resolution image corresponding to the petal tip area. d) The ADF intensity profile acquired along the blue region in (c). e) Schematic atomic model of the top-view (upper panel) and side-view (lower) of the crystalline structure associated to the crystallographic unit cell of 2H/3R polytype.

(the “stem”), see Figure 1e. The chemical composition of the WS_2 nanoflowers was confirmed by means of energy-dispersive X-ray spectroscopy (Figure S3, Supporting Information).

Figure 2a,b displays respectively low-magnification ADF- and bright-field (BF-) STEM images of the tip region of one representative WS_2 petal. The variations in image contrast indicates the presence of terraces with a different number of layers each, and thus of different thicknesses ranging from 2 nm up to 30 nm. Figure 2c then displays the atomic-resolution ADF-STEM image corresponding to the same petal. The petal has been oriented along the [0001] direction in order to ascertain the underlying crystalline structure. Each bright spot corresponds to an atomic column that is composed of alternating tungsten (W) and sulfur atoms.

Based on the observed atomic arrangement, a hexagonal honeycomb with an atom in its center, the atomic-resolution image appears to suggest a 3R phase (Figure S4b, Supporting Information). However, the ADF linescan extracted from the atomic resolution image across six lattice points (Figure 2d) indicates a threefold periodicity which is inconsistent with the 3R phase.

Such periodicity suggests instead a layer stacking order of the type BAA', characteristic of a mixture of the 2H (AA') and 3R (AB) phases.^[22] As displayed by the characteristic unit cell of polytypic 2H/3R (Figure 2e), the stacking sequence exhibits a broken inversion symmetry. Such polytypism has already been reported in related material like MoS_2 .^[12] As mentioned above, the 2H and 3R phases in their bilayer form are characterized by different stacking sequences, namely AA' and AB (Figure S4, Supporting Information). In the 2H phase, the W atom is aligned with the S one and the two layers exhibit inversion symmetry. In the 3R phase instead, the W atom is staggered over S, resulting in a stacking sequence lacking inversion symmetry. Therefore, a mixture of the two phases follows the BAA' sequence, where the third layer

is staggered with the S atoms over the W atoms of the second layer.

The area measured has a thickness of around 5 nm, which is equivalent to around 5 layers. The smallest thickness of any region in the specimen is found to be around 3 layers. ADF line profiles taken at different locations of other petals, corresponding to both single terraces and the transition region between terraces, exhibit in all cases the characteristic threefold periodicity of the 2H/3R polytype (see Figures S5 and S6, Supporting Information).

2. Fingerprinting Electronic Excitations with Spatially-Resolved EELS

The nature of collective electronic excitations such as surface and edge plasmons arising in the 2H/3R polytypism is investigated by means of spatially-resolved EELS. Figure 3a,b displays BF- and ADF-STEM images of horizontal WS_2 flakes (the nanoflower petals) overlapping among them. Some of these petals are composed by terraces of different thicknesses, as indicated by the contrast variations in the ADF-STEM image, Figure 3b. Since these petals are suspended on vacuum, it is possible to characterize their edge, surface, and bulk plasmons while reducing the contribution from coupling effects related to the nanostructure support film. It should be emphasized that, in this specific geometric configuration, the incident electron beam direction is close to the *c*-axis of the WS_2 petals.

Figure 3c displays the spatially-resolved EELS map recorded in the region marked with a grey rectangle in Figure 3b, where each pixel corresponds to the intensity of an individual EEL spectrum. Figure 3d,g displays the intensity maps associated to the same EEL signals now integrated in specific energy-loss windows: [2.5, 4.5], [8, 9], [12.5, 20], and [21.5, 25] eV respectively. In these maps,

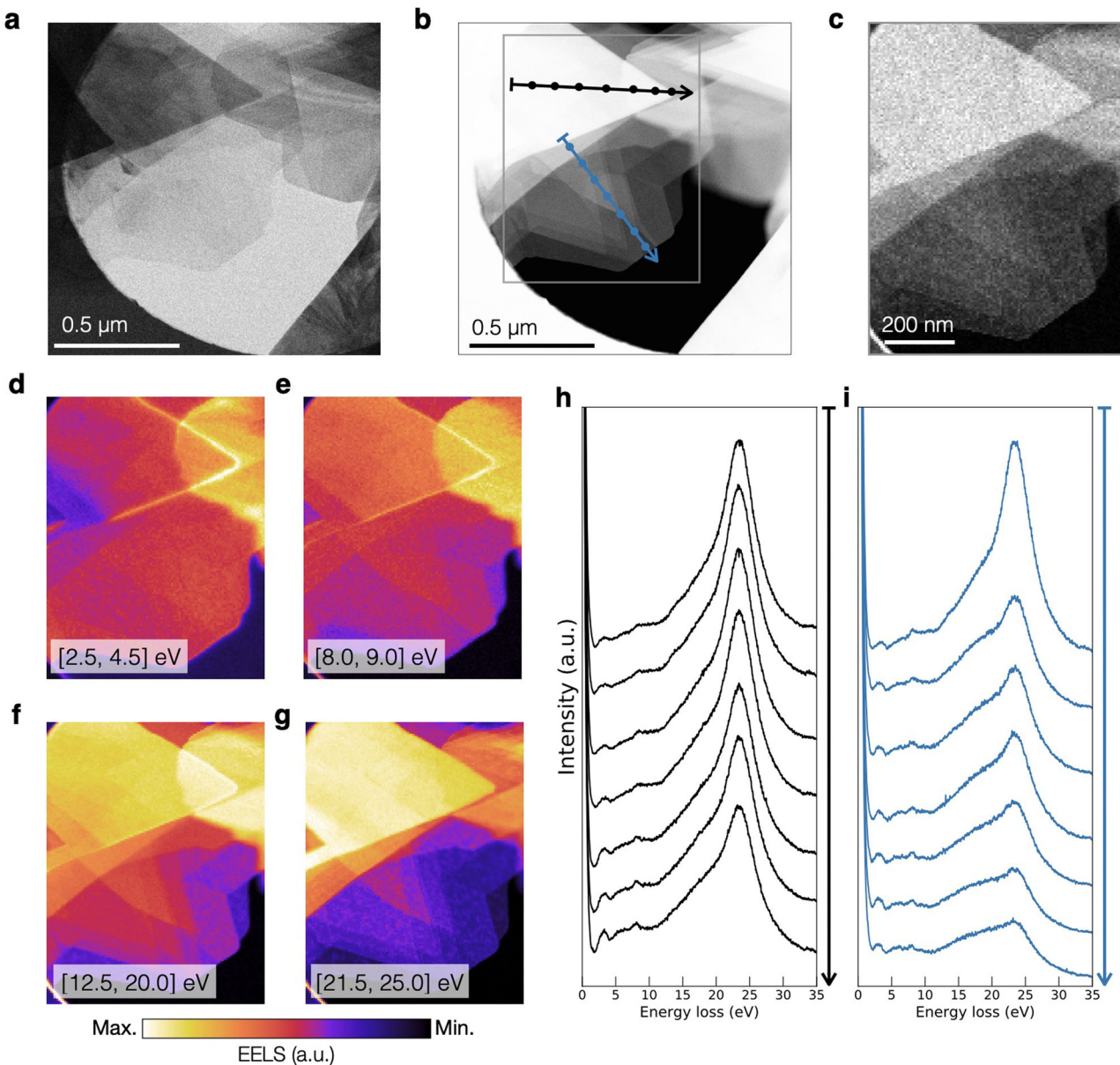


Figure 3. a,b) BF- and ADF-STEM images respectively of horizontal (flat) WS_2 petals. c) Spatially-resolved EELS map of the area indicated with a grey rectangle in (b). d–g) Intensity maps of the EELS signals integrated for different energy-loss windows. h,i) Individual EEL spectra taken at different locations along the horizontal petals as indicated by the black and blue arrows in (b). The spectra displayed in (h) correspond to a region characterized by the overlap of individual petals arising both from the left and the right sides of a,b. The spectra in (i) corresponds instead to a region displaying a petal composed by different terraces and thus different thicknesses.

the brighter regions highlight the dominant features appearing for each specific energy-loss range.

To better isolate the main features displayed by Figure 3d,g, representative EEL spectra associated to locations along the horizontal petals indicated in Figure 3b are presented in Figure 3h,i. A common feature of the two sets of spectra is the appearance of a prominent peak around 23 eV that can be associated with the WS_2 bulk plasmon.^[23] The intensity of this peak decreases as one moves from thicker towards thinner regions, following the directions of the arrows in Figure 3b. This effect is particularly

marked in Figure 3i, corresponding to a petal composed by terraces of different thicknesses.

From the intensity map corresponding to energy losses integrated between 12.5 and 20 eV, Figure 3f, one observes a significant contribution arising from the regions constituted by two different overlapping petals. The individual spectra display indeed a shoulder-like feature located around 17 eV, which becomes more marked in the thinner regions. The free-electron gas dielectric response theory predicts that the surface plasmon energy, E_s , should relate to that of the bulk one, E_p , by $E_s = E_p / \sqrt{2}$. In the

present case, this prediction corresponds to around $E_g = 16$ eV, consistent with the experimentally observed value and confirming the surface plasmon nature of this shoulder-like feature.^[9]

The individual spectra in Figure 3h,i also display less intense peaks located at energy losses around 3 and 8 eV. From the integrated EELS maps of Figure 3d, one observes that the 3 eV peak can be mainly associated to the edges of the WS₂ petals. Indeed, the largest signals in this energy-loss window arise from the tip of the edges and the adjacent regions. Further, it is observed that the peak at 8 eV receives its main contribution associated to the interlayer coupling between petals (Figure 3e). Indeed, this peak could be associated to the six π electrons (four of which are from the sulfur atoms) which are responsible for the interlayer interactions.^[24,25]

Figure 4a,b displays the ADF-STEM image and the corresponding spatially-resolved EELS map of another representative WS₂ nanoflower composed now by both flat and tilted WS₂ petals. In the latter case, their *c*-axis is close to being perpendicular to the direction of the electron beam. Figure 4c,d compares the energy-loss functions for the locations indicated in Figure 4b and recorded along a series of flat and tilted WS₂ petals respectively. Spectra 6, 9, and 10 in Figure 4b are recorded in vacuum but close enough to the petal (aloof configuration), in order to identify possible contributions from its surface plasmons. It is found that the 3 eV peak appears both in the flat and tilted petals, as well as in the vacuum location sp9. In the vacuum region close to the sample, a peak for energy losses of around 3 eV is observed, whose location shifts rightwards to 3.5 eV when moving from the non-penetrating (vacuum) to the penetrating (WS₂ petal) locations. To identify the physical nature of this feature a first principle density functional theory calculation (DFT) had been carried out, see Section SE, Supporting Information. The resulting total density of states (DOS) of 2H/3R WS₂ bulk is shown in Figure S7a, Supporting Information. By comparing the total DOS of W and S (Figure S7b,c, Supporting Information) one can see that the main contribution to the total DOS is attributed to the W atoms (Figure S7b, Supporting Information). In particular, it suggests that the peak around 3 eV is associated to electronic transitions from d states of W to unoccupied d states of W (see Figure S7, Supporting Information).

Concerning the higher-energy peaks, one finds that the tilted petal configuration induces a strong coupling between the surfaces which results in a split of the 17 eV surface mode into a peak at around 20 eV and a forest of peaks between 5 and 15 eV. In Figure 4d, a two-Gaussian model fit has been performed to sp1 (flat) and sp8 (tilted) in the range between 10 and 35 eV. The two resulting Gaussian distributions can be associated with the contributions from the bulk and surface plasmons and show how in the latter case the surface contribution at 17 eV blueshifts towards around 20 eV while becoming more marked as compared to the bulk one. Related phenomena have been reported in the case of WS₂ nanotubes with very small radii.^[23,26]

3. Band Gap Determination of Polytypic 2H/3R WS₂ from Machine Learning

The profile of the low-loss region of EEL spectra contains valuable information concerning the magnitude and type of the band gap. Exploiting this information requires the subtraction of the

zero-loss peak (ZLP) contribution. Here the band gap of polytypic 2H/3R WS₂ nanoflowers is investigated by means of a recently developed model-independent method based on machine learning.^[27] This approach, developed in the context of high energy physics,^[28] combines artificial neural networks for an unbiased parametrization of the ZLP profile with a Monte Carlo sampling for a faithful uncertainty estimate.

The original and subtracted EEL spectra corresponding to a representative location of a petal (labelled 5) and indicated in Figure S8, Supporting Information, are displayed in **Figure 5a** together with the calculated ZLP. This location corresponds to a relatively thick region where bulk behavior is expected. The uncertainty bands indicate the 68% confidence level intervals associated to the ZLP prediction and the subtracted spectrum. A functional form of the type $I_{EEL,sub}(\Delta E) = A \cdot (\Delta E - E_{BG})^b$ is then^[29] fitted to the subtracted spectrum ensuring that all relevant sources of uncertainty are considered. The results of such a fit are displayed in the inset of Figure 5a.

Figure 5b displays the ratio of the EELS intensity derivative, $dI_{ws2}/d(\Delta E)$ / $dI_{vac}/d(\Delta E)$ between the specimen spectrum and the corresponding vacuum average. This ratio highlights how for energy losses of 1.8 eV the two profiles start to differ, indicating the onset of the inelastic contributions to the spectra. The best-fit model values are $E_{BG} = 1.6^{+0.3}_{-0.2}$ eV for the band gap value and $b = 1.3^{+0.3}_{-0.4}$ for the exponent. The latter result favors an indirect band gap, for which $b \approx 3/2$ is theoretically expected. The obtained value and nature of the band gap of bulk WS₂ is consistent with previous determinations in the literature.^[8,14] Statistically comparable results for the model fits are obtained for other locations in Figure S8, Supporting Information.

4. Energy-Gain Peaks in EEL Spectra

Additional high-resolution EELS measurements in these nanostructures were carried out using a monochromated electron microscope (see the Experimental Section). **Figure 6a** displays the ZLP profile acquired in the vacuum; its full width at half maximum (FWHM), indicating the spectral resolution under these operational conditions, is 57 meV. The resulting EELS spectra recorded at three representative petals of the WS₂ nanoflowers are shown in Figure 6b-d. Each of these spectra corresponds to petals (displayed in the insets) characterized by different shape-morphology configurations: a flat petal tip (Figure 6b); a slightly bended petal (Figure 6c); and a completely bended petal (Figure 6d), respectively, where the darker contrast indicates bended regions.

These spectra exhibit both energy-gain ($\Delta E < 0$) and energy-loss ($\Delta E > 0$) peaks, distributed symmetrically about $\Delta E = 0$. The spectra in Figure 6b and 6c correspond to WS₂ petals oriented randomly, with the former being flat and the latter somewhat bended. From Figure 6b one finds symmetric peaks at $\Delta E = \pm 0.4$ and ± 0.6 eV and a shoulder-like structure at $\Delta E = \pm 0.2$ eV. A similar pattern is observed in the thicker, slightly bended specimen of Figure 6c, where again strong symmetric peaks are observed at $\Delta E = \pm 0.4$ eV but now the energy interval between the low-loss region peaks is around 0.4 eV. The spectrum displayed in Figure 6d corresponds instead to a completely bended petal. For this configuration, the symmetric peaks appear for $\Delta E = \pm 0.25$, ± 0.35 , and ± 0.6 eV. Since the positions of these peaks

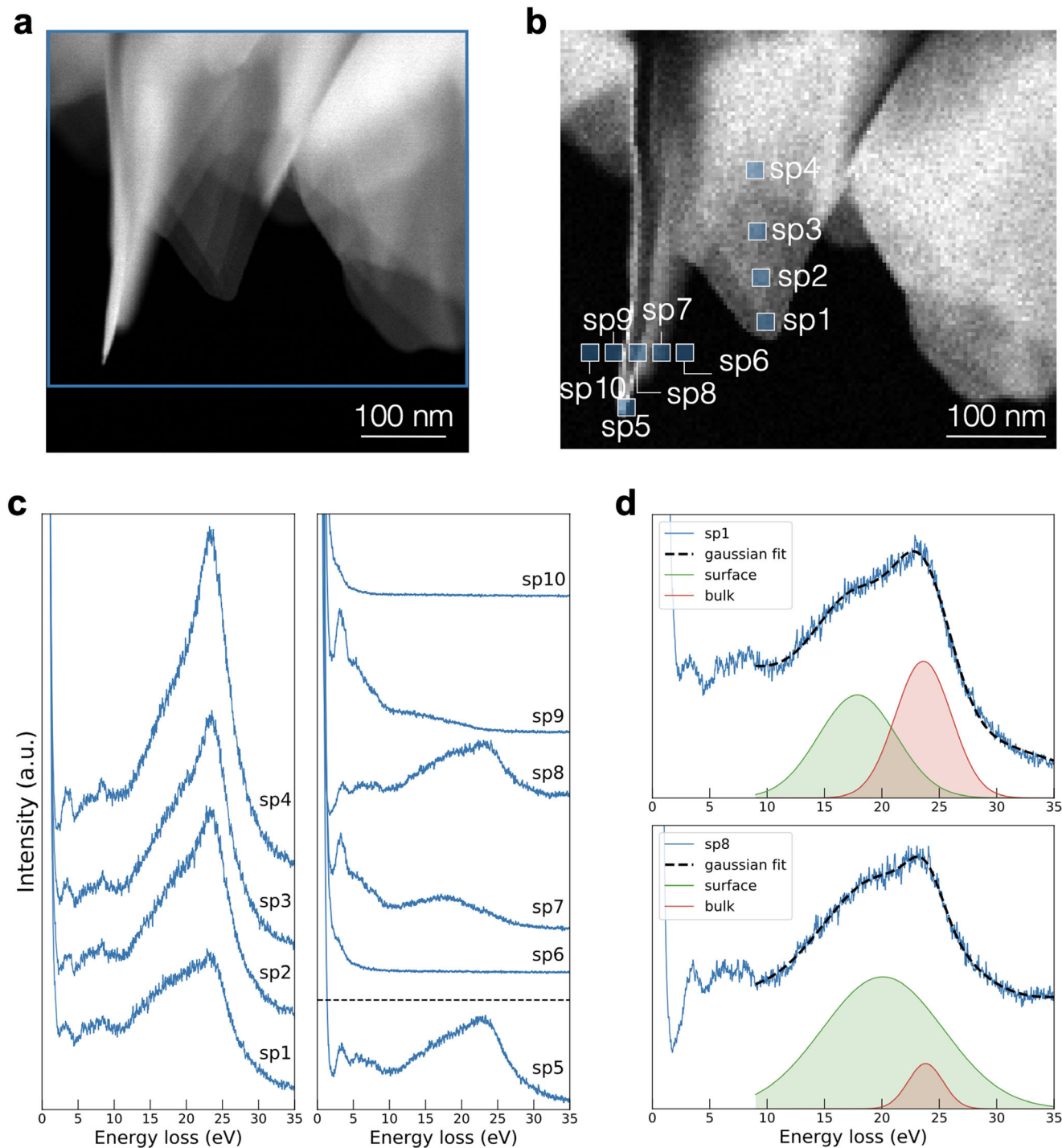


Figure 4. a) ADF-STEM image of another representative WS₂ nanostructure composed both by flat and tilted WS₂ petal. b) Spatially-resolved EELS map of the area indicated with a blue rectangle in (a). c) Individual EELS spectra corresponding to the locations indicated in (b). Spectra 1 to 4 are associated to a flat region of the WS₂ petal, while spectra 6 to 10 correspond to locations that cross the tilted WS₂ petal, with sp5 recorded at its tip. Note that sp6, 9, and 10 are recorded in vacuum but close enough to the petal to identify possible contributions from its surface plasmons. d) Spectra 1 and 8 where a two-Gaussian model fit has been performed in the range between 10 and 35 eV. The two resulting Gaussian distributions are also displayed and can be associated to the contributions from the bulk and surface plasmons.

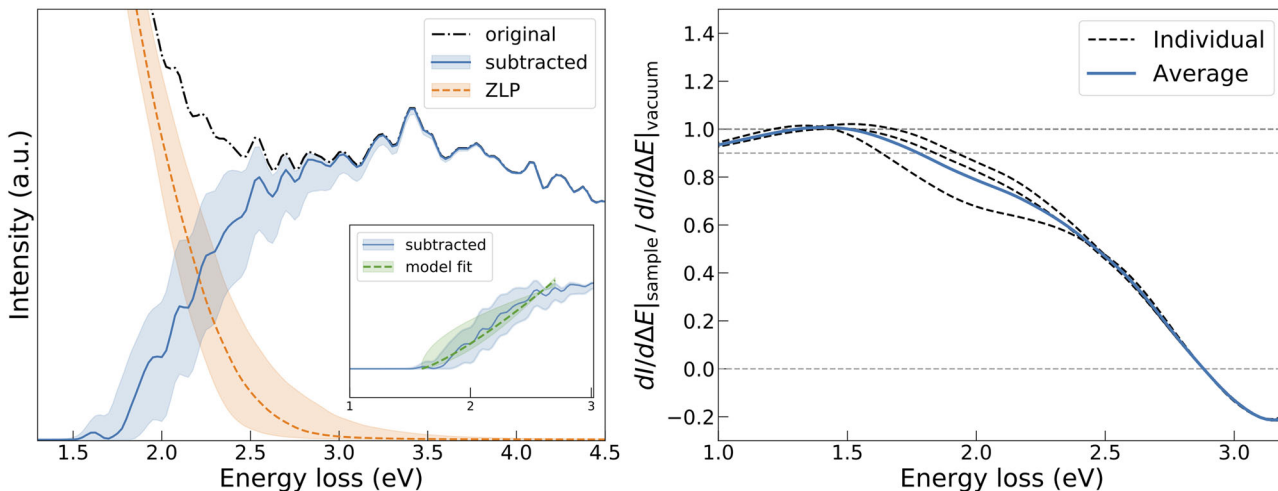


Figure 5. a) The low-loss region of the original EEL spectrum recorded at the location indicated in Figure S8, Supporting Information, together with the resulting subtracted spectrum. The ZLP model prediction used for the subtraction procedure is also displayed. The inset shows the result of the polynomial fit to the onset region of the subtracted spectrum and the bands represent the 68% CL intervals for the model uncertainties. b) The ratio of the derivative of the original EELS intensity profile indicated in (a) over the average of the corresponding derivative for spectra recorded in the vacuum. The value of the energy loss for which this ratio differs from unity by more than 10% determines the training range of the machine learning model. Note that this ratio crosses the x axis at the first local minimum of the unsubtracted spectrum.

does not correspond to the phonon resonances of WS_2 ,^[30] their origin could be associated to the interactions between the fast electron beam with the evanescent field that is created through the collective excitations of the WS_2 nanostructures.^[31] In this respect, work in progress based on ab initio calculations will shed more light on the underlying mechanism responsible for these gain/loss peaks.

The ratio between the gain and loss peak intensities, I_G/I_L , is known to depend on the relation between the associated thermal energies.^[32] From the spectra displayed in Figure 6b–d, one observes that this ratio is typically larger than one. Specifically, for the symmetric peaks closer to the ZLP in each spectrum, values of $I_G/I_L = 1.2$, 1.6 , and 1.5 are obtained, respectively. It is found that bended petals appear to exhibit larger gain/loss ratios than their flat counterparts. One should note that related features have been also observed in TMDs when studied by means of Raman scattering,^[33] where anomalously intense anti-Stokes peaks with $I_G/I_L > 1$ are reported. Such remarkable behavior could be exploited to develop novel cooling strategies for atomically thin TMD nanostructures and devices built upon them.

5. Conclusion

The understanding of the implications of unconventional mixed crystalline phases on the properties of TMD nanomaterials remains partially terra incognita. This work has presented the exhaustive characterization of WS_2 nanoflowers which provide an ideal laboratory for the study of the modifications of local electronic properties of WS_2 , thanks to their mixed 2H/3R polytypism and rich variety of shape-morphology configurations. By means of state-of-the-art AC-STEM and EELS measurements, the nature of their edge, surface, and bulk plasmonic excitations has been fingerprinted and the origin of distinctive features in the EELS spectra has been traced back to specific structural characteristics of the nanoflowers.

Further, thanks to a recently developed ZLP subtraction method based on machine learning, it has been established that the 2H/3R polytype of bulk WS_2 exhibits a semiconductor behavior with an indirect band gap of $E_{\text{BG}} = 1.6^{+0.3}_{-0.2}$ eV. Further, the presence of energy-gain peaks in the EELS spectra recorded in the WS_2 nanoflowers has been demonstrated. It has been shown that these peaks are characterized by a gain-to-loss ratio $I_G/I_L > 1$, indicating an underlying mechanism whereby electrons are on average accelerated after crossing the specimen. Such a feature could be exploited to develop novel cooling strategies for atomically thin TMD nanostructures and devices built upon them. This work therefore represents a stepping stone in a program aiming to develop a systematic strategy for the controllable growth of TMD nanostructures characterized by mixed crystalline phases.

6. Experimental Section

Electron Microscopy Characterization: The low magnification ADF image in Figure 1d and the EDS maps shown in Figure S3, Supporting Information, were taken using a Titan Cube microscope operated at 300 kV. The ADF- and BF-STEM and the EELS measurements displayed in Figures 1e, 2a–c, 3, and 4 were taken using a JEOL ARM200F microscope with a cold field-emission gun operated at 60 kV. This microscope is equipped with an aberration probe corrector and a Gatan GIF Quantum spectrometer. The convergence and collection semi-angles were set to 30.0 and 66.7 mrad, respectively. The spectral resolution (FWHM of the ZLP) achieved under these conditions is around 450 meV. The measurements in Figure 6 were collected in an ARM200F Mono-JEOL microscope equipped with a GIF continuum spectrometer. The microscope was operated at 200 kV in TEM mode with the monochromator ON and the smallest slit of 0.1 μm inserted. The aperture of the GIF was set to 1 mm. Under these conditions, one achieves a spectral resolution (FWHM) of 57 meV. In TEM-EELS the angular distribution of the electrons entering to the spectrometer aperture is independent of the entrance aperture size. The angular distribution is controlled by the size of the objective aperture in the diffraction pattern formed in the back focal plane of the objective

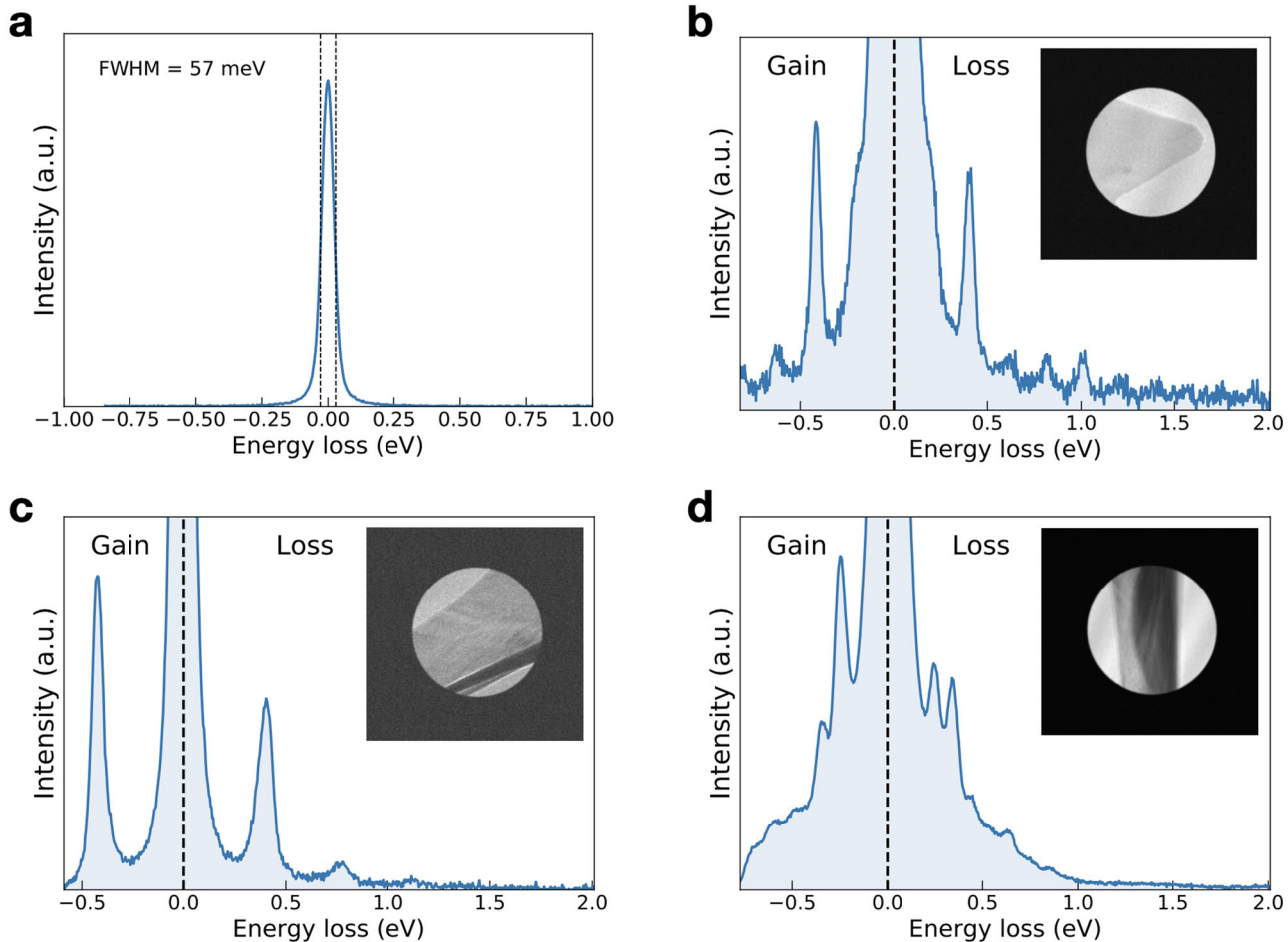


Figure 6. a) The ZLP recorded in the conventional TEM mode adopted for the vibrational spectroscopy measurements. The value of its FWHM indicates a spectral resolution (FWHM) of 57 meV. b,c,d) The electron energy gain/loss spectra for three representative WS_2 petals with different shape-morphology configurations: a flat petal tip (b); a slightly bended petal (c); and a completely bended petal (d) respectively. The insets display the TEM images for the area where each spectrum was recorded, where a darker contrast indicates a bended region of the petal. The gain/loss peaks appear symmetrically with respect to $\Delta E = 0$.

lens. For these measurements, an objective aperture of $40 \mu\text{m}$ was used, therefore the collection angle becomes around 6 mrad.

Supporting Information

Supporting Information is available from the Wiley Online Library or from the author.

Acknowledgements

The authors are grateful to Emanuele R. Nocera and Jacob J. Ethier for assistance in installing an EELSfitter in the Nikhef computing cluster. They also acknowledge discussions with Javier Garcia de Abajo on energy-gain phenomena in TMDs. S.E.v.H. and S.C.-B. acknowledge financial support from the ERC through the Starting Grant “TESLA”, grant agreement no. 805021. L.M. acknowledges support from the Netherlands Organizational for Scientific Research (NWO) through the Topconsortia voor Kennis en Innovatie (TKI) program. The work of J.R. has been partially supported by NWO.

Conflict of Interest

The authors declare no conflict of interest.

Keywords

machine learning methods, polytypes, transition metal dichalcogenides

Received: October 15, 2020

Revised: December 22, 2020

Published online:

- [1] D. Voiry, A. Mohite, M. Chhowalla, *Chem. Soc. Rev.* **2015**, *44*, 2702.
- [2] X. Zhang, Z. Lai, Q. Ma, H. Zhang, *Chem. Soc. Rev.* **2018**, *47*, 3301.
- [3] J. A. Wilson, A. D. Yoffe, *Adv. Phys.* **1969**, *18*, 193.
- [4] J. He, K. Hummer, C. Franchini, *Phys. Rev. B: Condens. Matter Mater. Phys.* **2014**, *89*, 075409.
- [5] R. Suzuki, M. Sakano, Y. J. Zhang, R. Akashi, D. Morikawa, A. Harasawa, K. Yaji, K. Kuroda, K. Miyamoto, T. Okuda, K. Ishizaka, R. Arita, Y. Iwasa, *Nat. Nanotechnol.* **2014**, *9*, 611.
- [6] D. Xiao, G.-B. Liu, W. Feng, X. Xu, W. Yao, *Phys. Rev. Lett.* **2012**, *108*, 196802.
- [7] J. Shi, P. Yu, F. Liu, P. He, R. Wang, L. Qin, J. Zhou, X. Li, J. Zhou, X. Sui, S. Zhang, Y. Zhang, Q. Zhang, T. C. Sum, X. Qiu, Z. Liu, X. Liu, *Adv. Mater.* **2017**, *29*, 1701486.

- [8] R. Yang, S. Feng, X. Lei, X. Mao, A. Nie, B. Wang, K. Luo, J. Xiang, F. Wen, C. Mu, Z. Zhao, B. Xu, H. Zeng, Y. Tian, Z. Liu, *Nanotechnology* **2019**, *30*, 345203.
- [9] P. Johari, V. B. Shenoy, *ACS Nano* **2011**, *5*, 5903.
- [10] C. Cong, J. Shang, X. Wu, B. Cao, N. Peimyoo, C. Qiu, L. Sun, T. Yu, *Adv. Opt. Mater.* **2014**, *2*, 131.
- [11] Y.-C. Lin, S. Li, H.-P. Komsa, L.-J. Chang, A. V. Krasheninnikov, G. Eda, K. Suenaga, *Adv. Funct. Mater.* **2018**, *28*, 1704210.
- [12] J.-U. Lee, K. Kim, S. Han, G. R. Ryu, Z. Lee, H. Cheong, *ACS Nano* **2016**, *10*, 1948.
- [13] R. J. Toh, Z. Sofer, J. Luxa, D. Sedmidubský, M. Pumera, *Chem. Commun.* **2017**, *53*, 3054.
- [14] Z. Zeng, X. Sun, D. Zhang, W. Zheng, X. Fan, M. He, L. Sun, X. Wang, *Adv. Funct. Mater.* **2019**, *29*, 1806874.
- [15] D. Tan, M. Willatzen, Z. L. Wang, *Nano Energy* **2019**, *56*, 512.
- [16] O. L. Krivanek, M. F. Chisholm, V. Nicolosi, T. J. Pennycook, G. J. Corbin, N. Dellby, M. F. Murfitt, C. S. Own, Z. S. Szilagyi, M. P. Oxley, S. T. Pantelides, S. J. Pennycook, *Nature* **2010**, *464*, 571.
- [17] O. L. Krivanek, T. C. Lovejoy, N. Dellby, T. Aoki, R. W. Carpenter, P. Rez, E. Soignard, J. Zhu, P. E. Batson, M. J. Lagos, R. F. Egerton, P. A. Crozier, *Nature* **2014**, *514*, 209.
- [18] J. A. Hunt, D. B. Williams, *Ultramicroscopy* **1991**, *38*, 47.
- [19] M. Mukai, E. Okunishi, M. Ashino, K. Omoto, T. Fukuda, A. Ikeda, K. Somehara, T. Kaneyama, T. Saitoh, T. Hirayama, Y. Ikuhara, *Microscopy* **2015**, *64*, 151.
- [20] M. Bolhuis, J. Hernandez-Rueda, S. E. van Heijst, M. T. Rivas, L. Kuipers, S. Conesa-Boj, *Nanoscale* **2020**, *12*, 10491.
- [21] M. O. Cichocka, M. Bolhuis, S. E. van Heijst, S. Conesa-Boj, *ACS Appl. Mater. Interfaces* **2020**, *12*, 15867.
- [22] A. Yan, W. Chen, C. Ophus, J. Ciston, Y. Lin, K. Persson, A. Zettl, *Phys. Rev. B* **2016**, *93*, 041420.
- [23] M. Kociak, O. Stéphan, L. Henrard, V. Charbois, A. Rothschild, R. Tenne, C. Colliex, *Phys. Rev. Lett.* **2001**, *87*, 075501.
- [24] W. Y. Liang, S. L. Cundy, *Philos. Mag.* **1969**, *19*, 1031.
- [25] K. Zeppenfeld, *Opt. Commun.* **1970**, *1*, 377.
- [26] D. Taverna, M. Kociak, V. Charbois, L. Henrard, *Phys. Rev. B* **2002**, *66*, 235419.
- [27] L. I. Roest, S. E. van Heijst, L. Maduro, J. Rojo, S. Conesa-Boj, arXiv:2009.05050 **2020**.
- [28] R. D. Ball, L. Del Debbio, S. Forte, A. Guffanti, J. I. Latorre, A. Piccione, J. Rojo, M. Ubiali, *Nucl. Phys. B* **2008**, *809*, 1.
- [29] B. Rafferty, L. M. Brown, *Phys. Rev. B* **1998**, *58*, 10326.
- [30] A. Molina-Sánchez, L. Wirtz, *Phys. Rev. B* **2011**, *84*, 155413.
- [31] F. J. Garcia de Abajo, M. Kociak, *New J. Phys.* **2008**, *10*, 073035.
- [32] J. C. Idrobo, A. R. Lupini, T. Feng, R. R. Unocic, F. S. Walden, D. S. Gardiner, T. C. Lovejoy, N. Dellby, S. T. Pantelides, O. L. Krivanek, *Phys. Rev. Lett.* **2018**, *120*, 095901.
- [33] T. Goldstein, S.-Y. Chen, J. Tong, D. Xiao, A. Ramasubramaniam, J. Yan, *Sci. Rep.* **2016**, *6*, 28024.